Supplementary Information

Deep-learning instance segmentation and explainable rule-based classification resolve platelets, red blood cells and aggregates in imaging flow cytometry

A.G. Wild, C. Venter, W.J. Perold, T.R. Niesler and E. Pretorius

Table S1: Comorbidities of Long COVID participants. No control participant reported any of these comorbidities, so the controls are omitted.

Comorbidity	**Long COVID participants (n=9)**
Rosacea	11 %
Type 1 diabetes	0 %
Type 2 diabetes	0 %
Periodontitis or gingivitis	0 %
Gut dysbiosis or leaky gut	0 %
High cholesterol	11 %
High blood pressure	0 %
Cardiovascular disease	0 %
Cancer	0 %
Psoriasis	0 %
Rheumatoid arthritis	0 %
Parkinson's disease	0 %
Alzheimer's disease	0 %

Spectral Compensation

	Ch01	Ch02	Ch03	Ch04	Ch05	Ch06	Ch07	Ch08	Ch09	Ch10	Ch11	Ch12
Ch01	1	0.105	0.045	0	0	0	0.003	0	0.002	0	0	0
Ch02	0.003	1	0.114	0	0	0	0.002	0	0.002	0	0	0
Ch03	0.004	0.214	1	0	0	0	0.002	0	0.005	0	0	0
Ch04	0	0.082	0.507	1	0	0	0.003	0	0	0	0	0
Ch05	0.002	0.023	0.154	0	1	0	0.003	0	0.002	0	0	0
Ch06	0.032	0.035	0.061	0	0	1	0.001	0	0.001	0	0	0
Ch07	0.006	0.019	0.017	0	0	0	1	0	0.023	0	0	0
Ch08	0.002	0.055	0.03	0	0	0	0.101	1	0.029	0	0	0
Ch09	0.002	0.014	0.118	0	0	0	0.015	0	1	0	0	0
Ch10	0.002	0.007	0.057	0	0	0	0.007	0	0.034	1	0	0
Ch11	0.002	0.004	0.023	0	0	0	0.004	0	0.025	0	1	0
Ch12	0.002	0.003	0.009	0	0	0	0.03	0	0.025	0	0	1

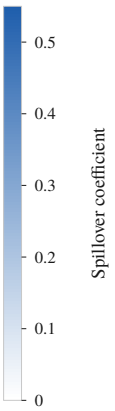


Figure S1: Compensation matrix of coefficients generated for the three fluorophores (Ch2: PAC-1, Ch3: CD62P and Ch7: CD235a) used to analyse the samples on the imaging flow cytometry (IFC).

Supplementary Note 1: Segmentation Model Training and Tuning

This section presents the architecture, training procedure and inference settings of the fine-tuned Cellpose3 model.

The Cellpose3 model is based on the U-net architecture [1]. Cellpose3 has four encoder and four decoder blocks, each with four residual convolutional layers. This amounts to a total of 32 convolutional layers. The architecture is discussed in detail in [2]. The IFC image dataset was split into 8076 training and 2016 held-out images. The split was made at the image level. Images from the same acquisition may therefore occur in both splits. Cellpose3 was fine-tuned on the training split for 100 epochs with the AdamW optimizer [3]. AdamW is the Adam optimizer with weight decay decoupled from the gradient update. The learning rate was increased linearly from 0 to 0.005 over the first 10 epochs and then held constant. The weight decay was 10^{-5} and the batch size was 16. Training images were augmented by random rotation and by random rescaling within a factor of 0.5, using the Cellpose `random_rotate_and_resize` function. The batch order was seeded with the epoch number. The checkpoint with the lowest loss on the held-out images was retained. Training used Cellpose 3 and PyTorch on a single GPU of a high-performance computing cluster.

The inference settings are listed in Table S2.

Table S2: Inference settings of the fine-tuned Cellpose3 model. The same settings were used for the held-out images and the study samples. Settings not listed were left at the Cellpose 3.0.9 default.

Setting	**Value used**
Input channel	Brightfield, greyscale
Intensity normalisation	1st to 99th percentile per image
Cell diameter	8.05 px, the mean of the training masks
Rescale factor	$30/8.05 \approx 3.73$
Flow error threshold	0.4
Cell probability threshold	0.0
Minimum mask size	15 px
Dynamics iterations	$200/3.73 \approx 54$
Flows resampled to input size	Yes
Tile size and overlap	224 px, 0.1
Test-time augmentation	No
Batch size	512

Supplementary Note 2: Classification Thresholds

This section gives the reasoning behind the thresholds of the population classification.

If the mask is large and has an `equivalent_diameter` ≥ 8 px, then the mask is likely a red blood cell (RBC). The size thresholds were set between the mask sizes of the two cell types. Median platelet masks have an equivalent diameter of about 5 px. Median RBC masks have an equivalent diameter of about 9 px. Brightfield masks are larger than the cells at this pixel size. At $1\,\mu$m per pixel, the median RBC mask has an area of $66\,\mu m^2$. Cell size is not solely judged on `equivalent_diameter`. RBCs are biconcave disks and do not always appear face-on to the camera. RBCs viewed at an oblique angle appear as ellipses with a reduced area, and hence an `equivalent_diameter` that may overlap with the platelet population. Therefore, the `major_axis` is also incorporated into the size measurement. The `major_axis` of such a mask retains the full RBC diameter. The lower `major_axis` threshold of 7 px favors RBC recall, so round platelet masks with a major axis between 7 px and 8 px may be classified as RBC-like. Fully side-on RBCs, however, are too elongated to pass the eccentricity rule and are assigned to the irregular population. Furthermore, the CD235a median intensity is intended to save additional RBCs seen at an unfavorable orientation from being placed in the platelet population. CD235a was not added to the platelet-rich plasma (PRP) fraction, so this rule is inactive for PRP.

A `solidity` threshold of 0.88 was chosen based on the empirical distribution of the high-yield platelet optimization (HPO) masks, with $P_5 = 0.87$ and $P_{50} = 0.94$. A threshold of 0.88, just above P_5, retains 93% of these masks, while rejecting fragmented and multi-blob masks. Eccentricity is a measure of how elongated a mask is. A circle has an `eccentricity` of 0, while a line has a value of 1. An `eccentricity` threshold of 0.85 describes cells that are roughly twice as long as they are wide.

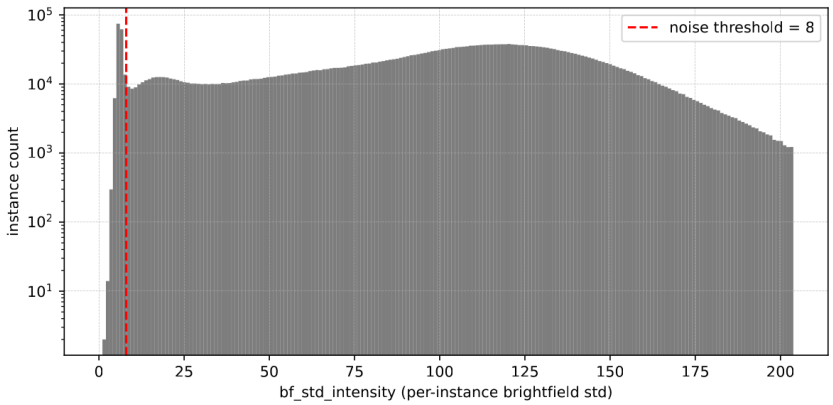


Figure S2: Noise filter applied to all brightfield masks. Masks with a standard deviation of brightfield intensity below 8 are removed.

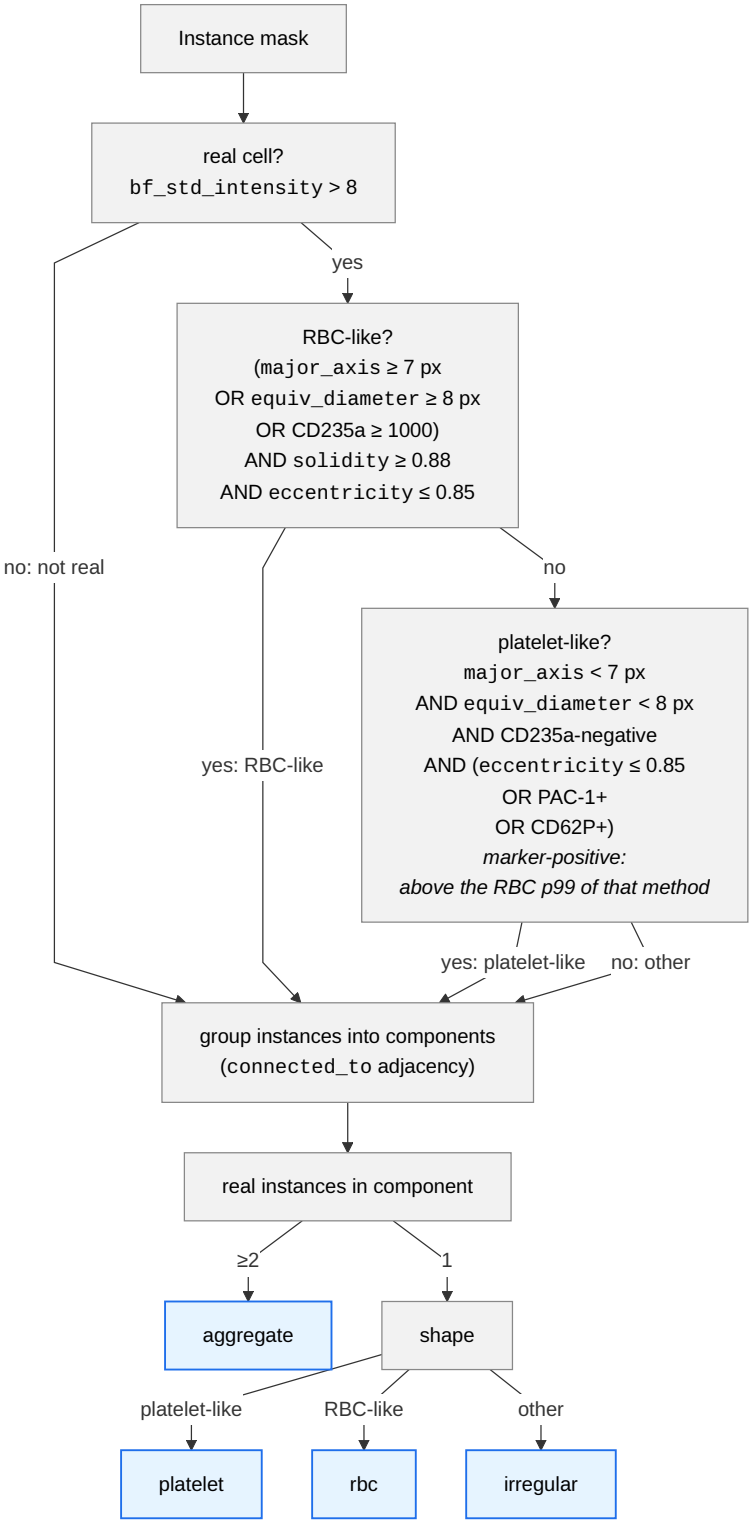


Figure S3: Population classification logic displayed as a decision tree.

Table S3: Per-particle features extracted from each segmented object. Geometric and spatial features are derived once per object from the brightfield mask. Texture and intensity features are computed for every acquired channel through the same mask.

Group	Feature	Description
Geometric	`area`	Number of pixels inside the object mask.
	`perimeter`	Length of the object boundary.
	`bbox_w`	Bounding-box width.
	`bbox_h`	Bounding-box height.
	`convex_area`	Area of the convex hull of the mask.
	`circularity`	$4\pi \cdot \text{area}/\text{perimeter}^2$; 1 for a circle.
	`solidity`	area/convex_area; concavity measure.
	`eccentricity`	Eccentricity of the fitted ellipse (0=circle, 1=line).
	`aspect_ratio`	Major-axis length divided by minor-axis length.
	`major_axis_length`	Length of the fitted ellipse major axis.
	`minor_axis_length`	Length of the fitted ellipse minor axis.
	`orientation`	Angle of the major axis w.r.t. the x-axis.
	`equivalent_diameter`	Diameter of a circle with equal area.
	`extent`	area divided by bounding-box area.
Spatial	`centroid_x`	x-coordinate of the mask centroid.
	`centroid_y`	y-coordinate of the mask centroid.
	`bbox_x`	x of the bounding-box top-left corner.
	`bbox_y`	y of the bounding-box top-left corner.
	`distance_to_edge`	Shortest distance from centroid to image border.
	`connected_to`	Id(s) of the neighboring object(s) the mask touches (if any).
Texture	`gradient_rms`	Root-mean-square Sobel gradient magnitude inside the mask (focus / sharpness).
	`glcm_contrast`	GLCM contrast: local intensity variation.
	`glcm_homogeneity`	GLCM homogeneity: closeness of element distribution to the diagonal.
	`glcm_energy`	GLCM energy: sum of squared elements (uniformity).
	`glcm_correlation`	GLCM correlation between neighboring pixel intensities.
	`glcm_dissimilarity`	GLCM dissimilarity: mean absolute intensity difference.
Intensity	`mean_intensity`	Mean pixel intensity inside the mask.
	`std_intensity`	Standard deviation of intensities inside the mask.
	`min_intensity`	Minimum pixel intensity inside the mask.
	`max_intensity`	Maximum pixel intensity inside the mask.
	`median_intensity`	Median pixel intensity inside the mask.
	`integrated_intensity`	Sum of pixel intensities inside the mask.

Representative Events

Representative events of each population are shown in Fig. S4, Fig. S5 and Fig. S6. The events were selected from the HPO fraction of both cohorts. Every mask instance is drawn in its own color. PAC -1, CD62P and CD235a are displayed with the viridis, magma and inferno color maps, respectively. Fluorescence is shown on an arcsinh scale with one fixed display range per channel. The same display is used for all events, so intensities may be compared between events.

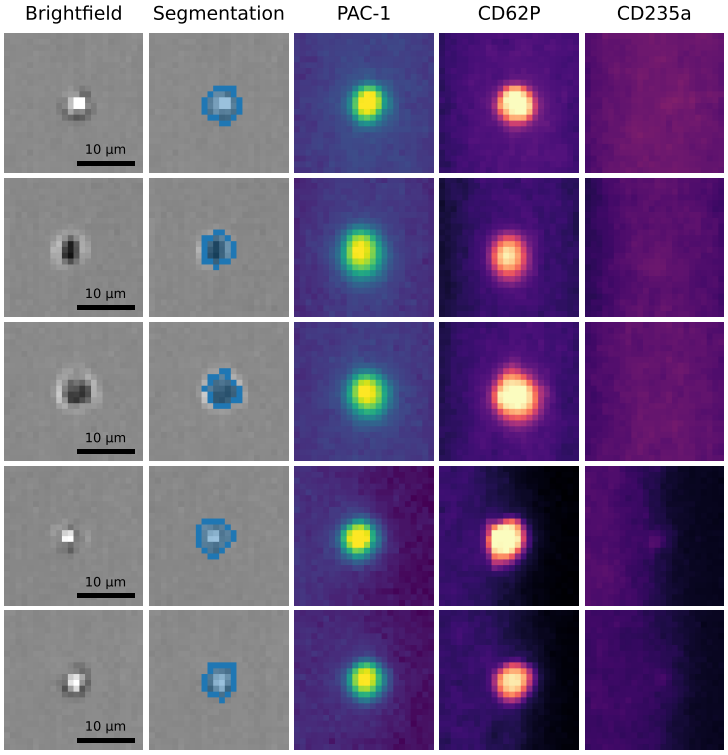


Figure S4: Representative events of the platelet population in the HPO fraction. Each row is one event. The columns show the brightfield image, the instance segmentation masks and the PAC-1, CD62P and CD235a channels. The scale bars are 10 µm.

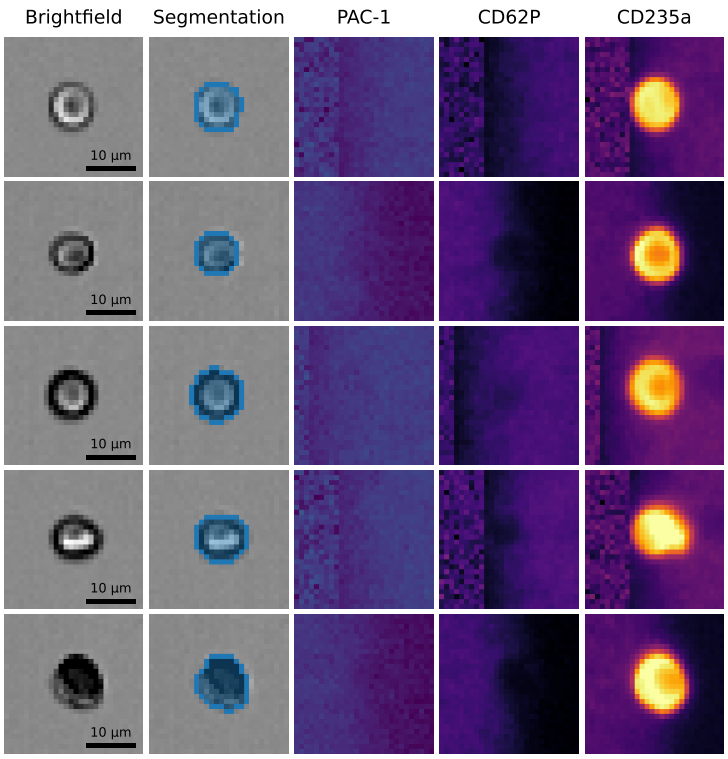


Figure S5: Representative events of the RBC population in the HPO fraction. Each row is one event. The columns show the brightfield image, the instance segmentation masks and the PAC-1, CD62P and CD235a channels. The scale bars are 10 µm.

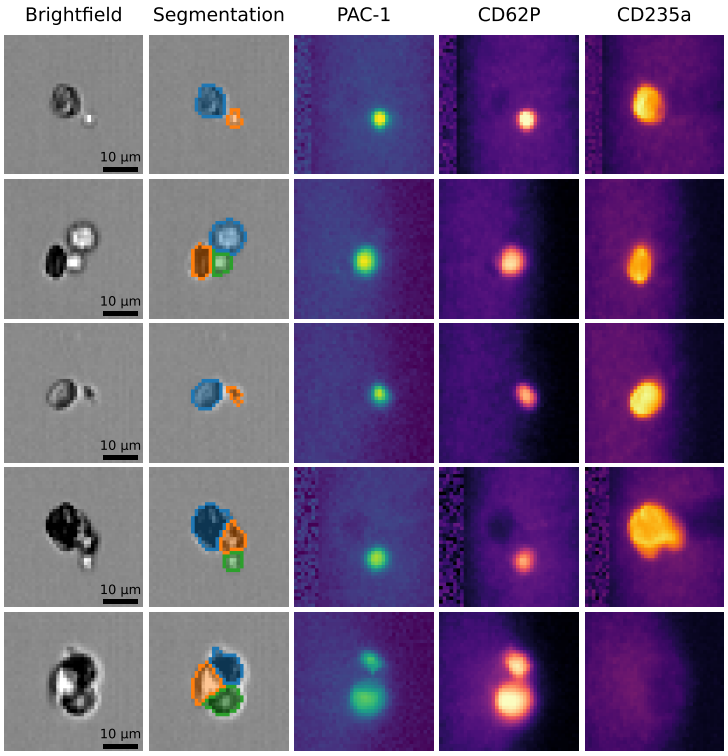


Figure S6: Representative events of the aggregate population in the HPO fraction. Each row is one event. The columns show the brightfield image, the instance segmentation masks and the PAC-1, CD62P and CD235a channels. The scale bars are 10 µm.

Inter-Annotator Validation Set

The 50 images of the inter-annotator validation set are shown in Fig. S7. Table S4 gives the pipeline class and the human consensus label of every image.

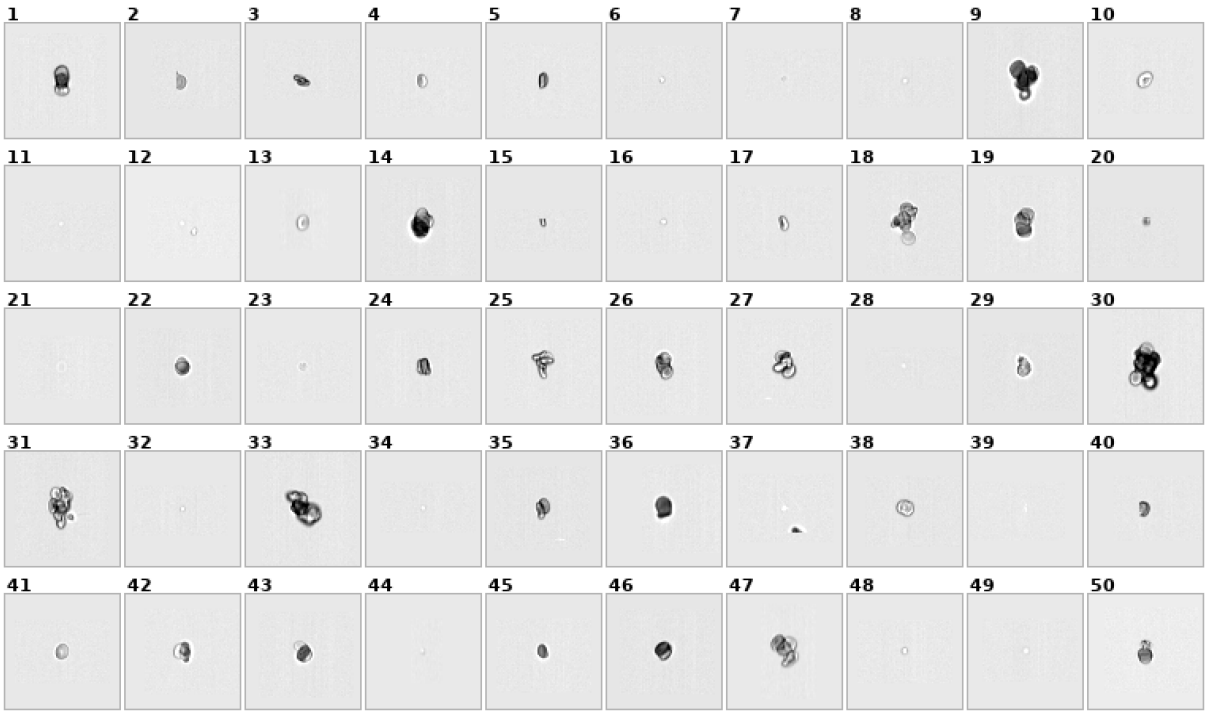


Figure S7: The 50 brightfield images of the inter-annotator validation set. Each image is enlarged six times with no smoothing. The images were sampled from both cohorts of the HPO preparation method. Sampling was stratified by the class assigned by the classification pipeline. The annotators classified the central object of each image.

Table S4: Pipeline class and human consensus label of the 50 images of the inter-annotator validation set. The image numbers follow Fig. S7. Pip. is the pipeline class and Con. is the consensus label. P denotes platelet, R denotes RBC and A denotes aggregate. The consensus label is the majority vote of the five human annotators. Images where the pipeline and the consensus differ are shown in bold.

No.	Pip.	Con.	No.	Pip.	Con.	No.	Pip.	Con.	No.	Pip.	Con.	No.	Pip.	Con.
1	A	A	11	P	P	**21**	**R**	**P**	31	A	A	41	R	R
2	R	R	12	P	P	22	R	R	32	P	P	42	A	A
3	A	A	13	R	R	23	P	P	33	A	A	43	A	A
4	R	R	14	A	A	24	R	R	34	P	P	44	P	P
5	R	R	15	P	P	25	A	A	**35**	**R**	**A**	45	R	R
6	P	P	16	P	P	26	A	A	36	R	R	46	R	R
7	P	P	17	R	R	27	A	A	37	P	P	47	A	A
8	P	P	18	A	A	28	P	P	38	R	R	48	P	P
9	A	A	19	A	A	29	R	R	39	P	P	49	P	P
10	R	R	20	P	P	30	A	A	40	R	R	50	A	A

Table S5: Comparison of the primary and exploratory endpoints between the control and Long COVID cohorts. p_{BH} is the Benjamini–Hochberg adjusted p-value across the four endpoints within each method and population, except for the HPO concentrations, which are corrected across the three populations; effect sizes are Cliff's δ with Romano *et al*. magnitudes.

Endpoint	Method	Population	Control median	Long COVID median	Cliff's δ	Effect magnitude	p_{BH}
Concentration (obj/µL)	HPO	Platelet	616	1147	0.64	Large	0.019
		RBC	2321	10 196	0.98	Large	<0.001
		Aggregate	1382	2202	0.72	Large	0.012
	Hematocrit	Platelet	1859	2177	0.21	Small	0.597
		RBC	45 039	49 466	−0.03	Negligible	0.939
		Aggregate	8312	9907	−0.09	Negligible	0.820
	PRP	Platelet	15 720	32 177	0.70	Large	0.039
		RBC	2678	3474	0.58	Large	0.066
		Aggregate	317	688	0.68	Large	0.036
	WB	Platelet	925	1147	0.49	Large	0.091
		RBC	20 279	21 391	−0.01	Negligible	1.000
		Aggregate	4581	5270	0.58	Large	0.045
Absolute count	HPO	Platelet	7995	15 024	0.64	Large	0.037
		RBC	30 640	133 251	0.98	Large	<0.001
		Aggregate	18 003	28 781	0.72	Large	0.016
	Hematocrit	Platelet	9115	10 562	0.39	Medium	0.298
		RBC	237 669	245 295	0.21	Small	0.893
		Aggregate	41 642	47 722	0.19	Small	0.820
	PRP	Platelet	103 689	137 286	0.41	Medium	0.172
		RBC	20 170	21 933	0.15	Small	0.595
		Aggregate	2423	3198	0.47	Large	0.081
	WB	Platelet	9452	11 906	0.66	Large	0.030
		RBC	202 983	203 512	0.05	Negligible	1.000
		Aggregate	39 605	56 112	0.58	Large	0.045
% of total	HPO	Platelet	13.2	8.23	−0.45	Medium	0.126
		RBC	57.4	73.6	0.45	Medium	0.126
		Aggregate	28.9	17.3	−0.52	Large	0.077
	Hematocrit	Platelet	3.20	3.61	0.39	Medium	0.298
		RBC	81.7	80.6	−0.17	Small	0.893
		Aggregate	15.5	15.6	−0.07	Negligible	0.820
	PRP	Platelet	82.9	87.4	0.49	Large	0.136
		RBC	15.2	10.2	−0.66	Large	0.060
		Aggregate	1.76	2.15	0.49	Large	0.081
	WB	Platelet	3.61	4.68	0.76	Large	0.020
		RBC	80.0	74.2	−0.54	Large	0.193
		Aggregate	16.4	18.5	0.41	Medium	0.129
Median area (µm^2)	HPO	Platelet	22.0	27.0	0.35	Medium	0.181
		RBC	66.0	66.0	0.00	Negligible	1.000
		Aggregate	155	188	0.29	Small	0.287
	Hematocrit	Platelet	21.0	21.0	0.02	Negligible	0.942
		RBC	63.2	63.2	−0.12	Negligible	0.893
		Aggregate	118	116	−0.40	Medium	0.542
	PRP	Platelet	21.0	22.0	0.19	Small	0.454
		RBC	35.0	33.0	−0.53	Large	0.066
		Aggregate	48.0	44.0	−0.64	Large	0.036
	WB	Platelet	22.0	22.0	0.02	Negligible	0.962
		RBC	66.0	66.0	−0.36	Medium	0.325
		Aggregate	114	108	−0.63	Large	0.045

Fluorescence Micrographs

Fluorescence micrographs of the four preparation methods are provided as a qualitative illustration of the PRP, hematocrit, HPO and whole blood (WB) fractions. Platelets are indicated by the green PAC-1 and pink CD62P signals, and RBCs by the blue CD235a signal. The micrographs were not blinded or quantified.

Figure S8 shows platelets prepared from PRP. In this fraction, platelets from control participants showed minimal pseudopodia formation and no platelet clumping, whereas platelets from Long COVID participants showed minimal pseudopodia formation and some platelet spreading. PRP is the standard technique to prepare platelets for analysis, and is typically used by pathology laboratories [4]. However, there were minimal differences between the control and Long COVID platelets in the PRP micrographs.

Figure S9 shows platelets from the standard hematocrit fraction. Substantial platelet activation in participants with both acute COVID-19 and Long COVID has previously been reported with this method [5–10]. In this study, activated platelets were seen in the Long COVID participants, with more pseudopodia and platelet spreading than in the controls, which showed minimal platelet activation. Figure S10 shows platelets from the HPO fraction, with more platelet activation in the Long COVID participants and minimal activation in the control samples. Figure S11 shows the WB fraction, in which activated platelets were seen in both the control and Long COVID participants. Why WB platelets appear activated in the micrographs, but showed no platelet marker signal in IFC, requires further investigation.

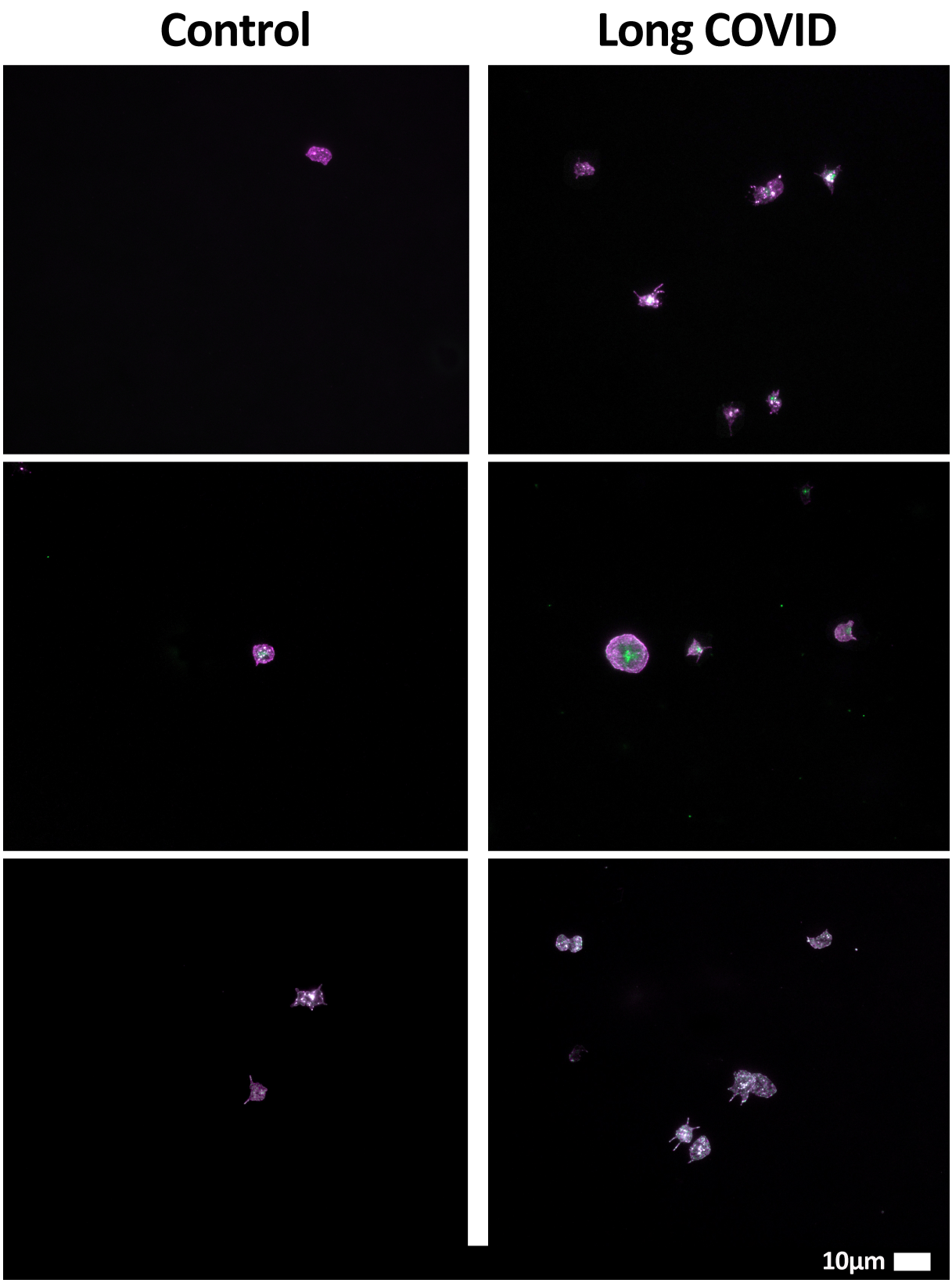


Figure S8: Representative fluorescence micrographs of platelets in the PRP fraction of control and Long COVID participants, with 10 µm scale bars. PRP was stained with PAC-1, green, and CD62P, pink.

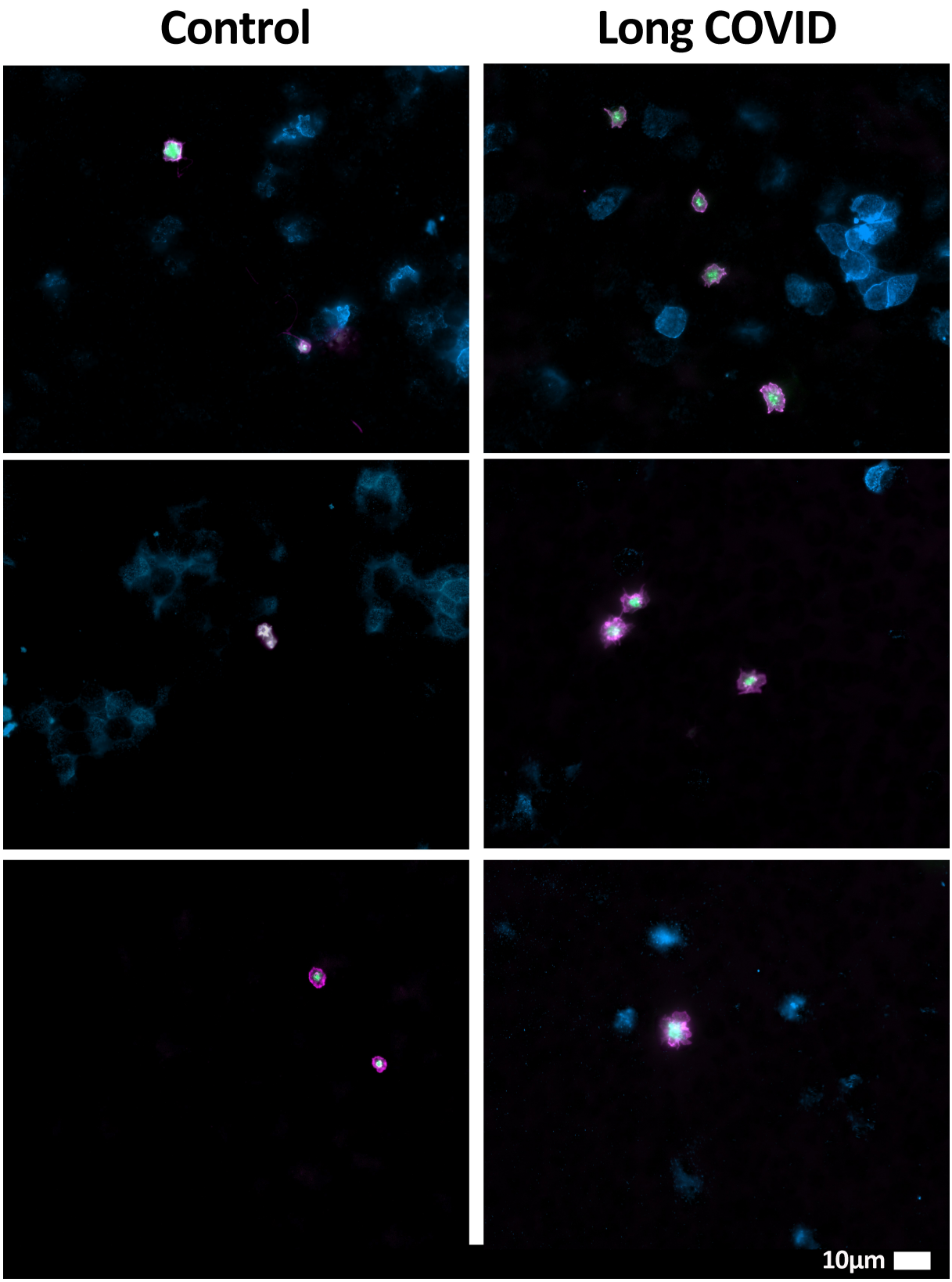


Figure S9: Representative fluorescence micrographs of platelets in the hematocrit fraction of control and Long COVID participants, with 10 µm scale bars. The hematocrit was stained with PAC-1, green, CD62P, pink, and CD235a, blue.

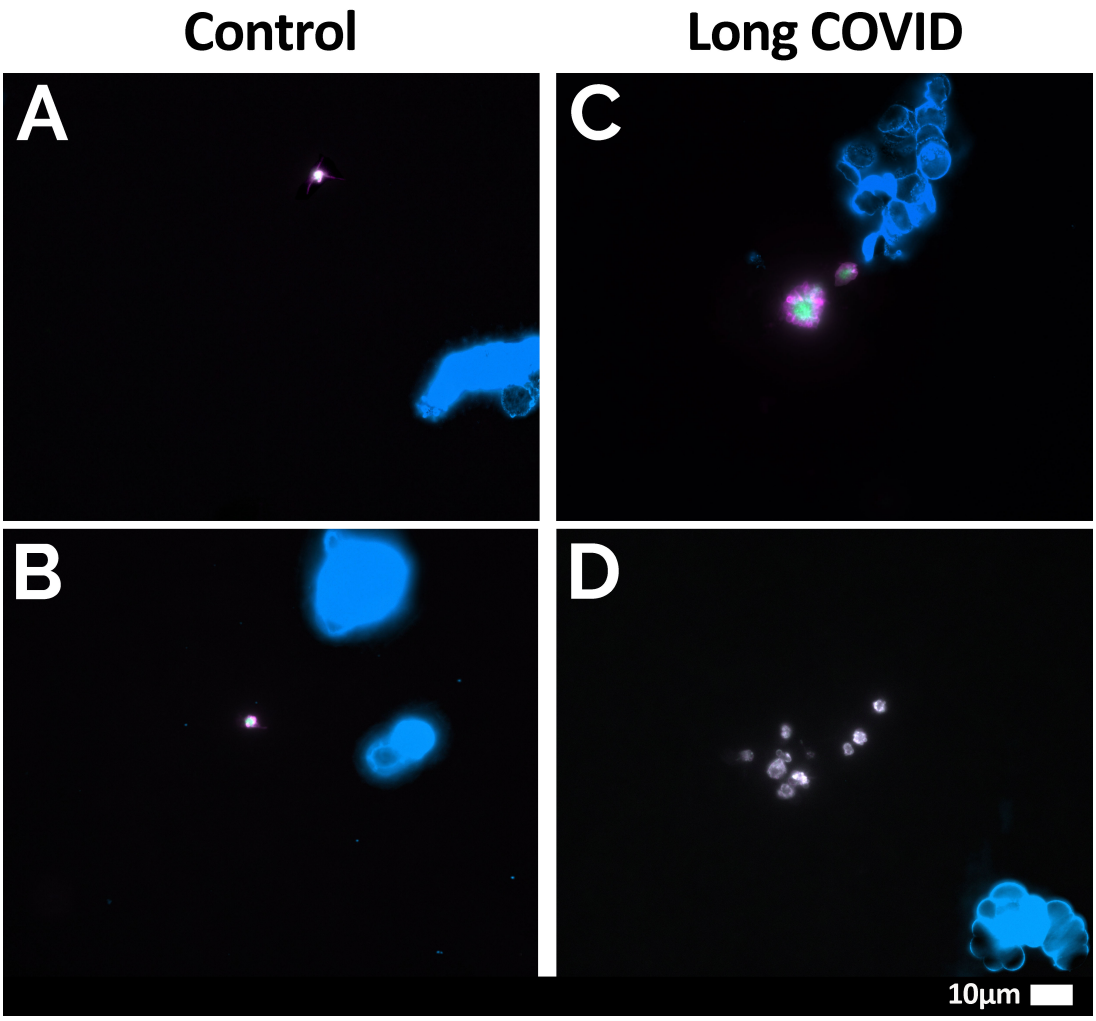


Figure S10: Representative fluorescence micrographs of the HPO fraction, with 10 µm scale bars. A and B show control samples. C and D show Long COVID samples.

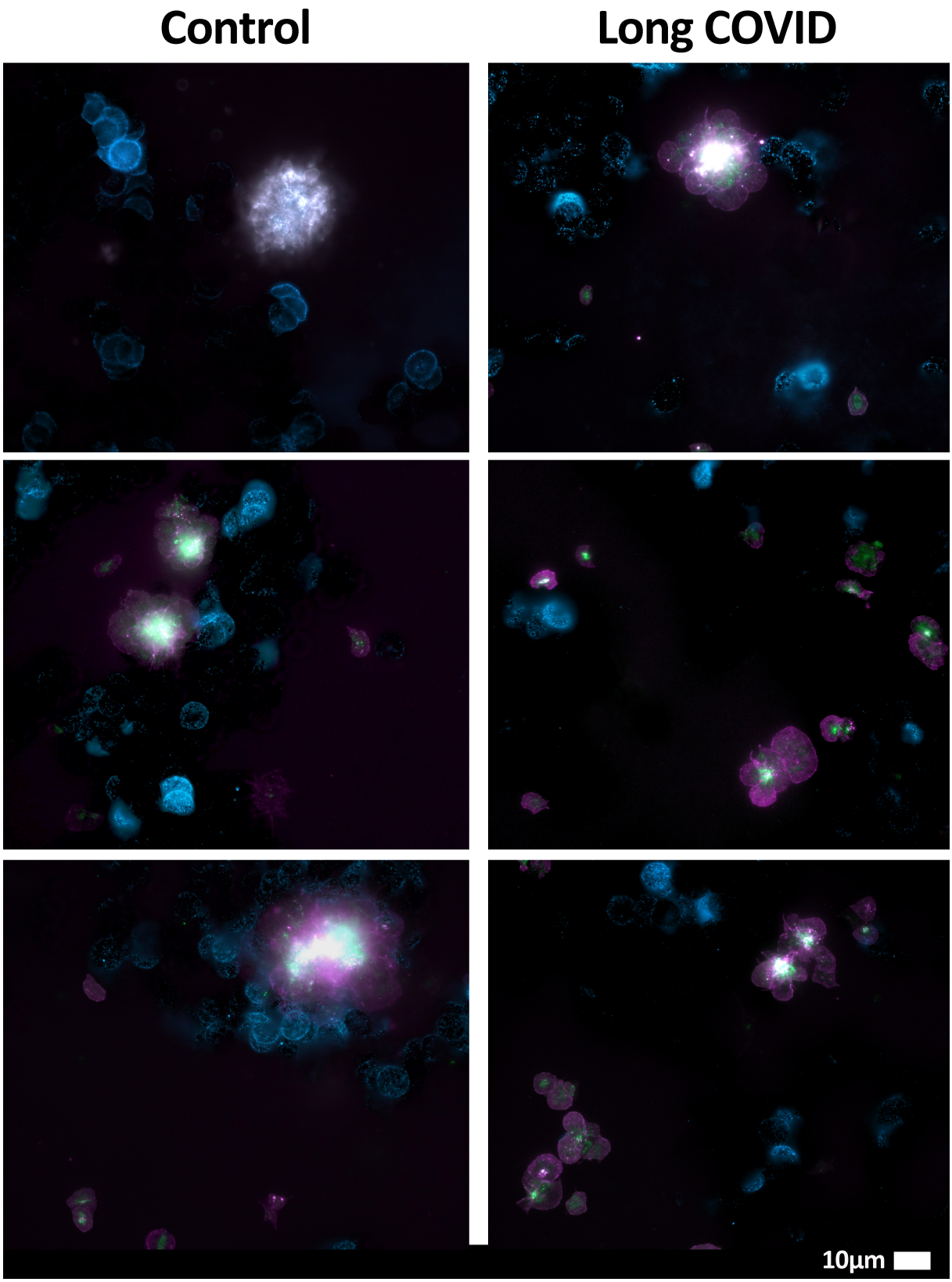


Figure S11: Representative fluorescence micrographs of platelets in the WB fraction of control and Long COVID participants, with 10 µm scale bars. WB was stained with PAC-1, green, CD62P, pink, and CD235a, blue.

Author Contributions

The roles of each author follow the CRediT taxonomy and are listed in Table S6.

Table S6: Contributions of each author according to the CRediT taxonomy.

CRediT role	A.G. Wild	C. Venter	E. Pretorius	W.J. Perold	T.R. Niesler
Conceptualization	•	•	•		
Data curation	•				
Formal analysis	•				
Funding acquisition			•		
Investigation		•			
Methodology	•	•	•		
Project administration		•	•		
Resources	•		•		
Software	•				
Supervision			•	•	•
Validation	•				
Visualization	•	•			
Writing – original draft	•	•	•		
Writing – review & editing	•	•	•		•

References

[1] O. Ronneberger, P. Fischer, and T. Brox, "U-Net: convolutional networks for biomedical image segmentation," *Medical Image Computing and Computer-Assisted Intervention – MICCAI 2015*, vol. 9351, pp. 234–241, 2015.

[2] C. Stringer, T. Wang, M. Michaelos, and M. Pachitariu, "Cellpose: a generalist algorithm for cellular segmentation," *Nature Methods*, vol. 18, no. 1, pp. 100–106, 2021.

[3] I. Loshchilov and F. Hutter, "Decoupled weight decay regularization," *Proceedings of the International Conference on Learning Representations*, 2019.

[4] K. Althaus, L. Pelzl, O. Hidiatov, J. Amiral, I. Marini, and T. Bakchoul, "Evaluation of a flow cytometer-based functional assay using platelet-rich plasma in the diagnosis of heparin-induced thrombocytopenia," *Thrombosis Research*, vol. 180, pp. 55–61, 2019.

[5] C. Venter, J. A. Bezuidenhout, G. J. Laubscher, P. J. Lourens, J. Steenkamp, D. B. Kell, and E. Pretorius, "Erythrocyte, platelet, serum ferritin, and P-selectin pathophysiology implicated in severe hypercoagulation and vascular complications in COVID-19," *International Journal of Molecular Sciences*, vol. 21, no. 21, p. 8234, 2020.

[6] E. Pretorius, M. Vlok, C. Venter, J. A. Bezuidenhout, G. J. Laubscher, J. Steenkamp, and D. B. Kell, "Persistent clotting protein pathology in Long COVID/Post-Acute Sequelae of COVID-19 (PASC) is accompanied by increased levels of antiplasmin," *Cardiovascular Diabetology*, vol. 20, no. 1, p. 172, 2021.

[7] E. Pretorius, C. Venter, G. J. Laubscher, P. J. Lourens, J. Steenkamp, and D. B. Kell, "Prevalence of readily detected amyloid blood clots in 'unclotted' Type 2 Diabetes Mellitus and COVID-19 plasma: a preliminary report," *Cardiovascular Diabetology*, vol. 19, p. 193, 2020.

[8] E. Pretorius, C. Venter, G. J. Laubscher, M. J. Kotze, S. O. Oladejo, L. R. Watson, K. Rajaratnam, B. W. Watson, and D. B. Kell, "Prevalence of symptoms, comorbidities, fibrin amyloid microclots and platelet pathology in individuals with Long COVID/Post-Acute Sequelae of COVID-19 (PASC)," *Cardiovascular Diabetology*, vol. 21, p. 148, 2022.

[9] G. J. Laubscher, P. J. Lourens, C. Venter, D. B. Kell, and E. Pretorius, "TEG®, microclot and platelet mapping for guiding early management of severe COVID-19 coagulopathy," *Journal of Clinical Medicine*, vol. 10, no. 22, p. 5381, 2021.

[10] C. Grobler, S. C. Maphumulo, L. M. Grobbelaar, J. C. Bredenkamp, G. J. Laubscher, P. J. Lourens, J. Steenkamp, D. B. Kell, and E. Pretorius, "Covid-19: the rollercoaster of fibrin(ogen), D-dimer, von Willebrand factor, P-selectin and their interactions with endothelial cells, platelets and erythrocytes," *International Journal of Molecular Sciences*, vol. 21, no. 14, p. 5168, 2020.

Supplementary Note: MIFlowCyt checklist

Minimum Information about a Flow Cytometry Experiment (Lee *et al.*, Cytometry A 2008;73:926–930)

Manuscript: Deep-learning instance segmentation and explainable rule-based classification resolve platelets, red blood cells and aggregates in imaging flow cytometry

Authors: A.G. Wild, C. Venter, W.J. Perold, T.R. Niesler and E. Pretorius

Version: 1 October 2026. Locations refer to the headings of the manuscript. SI = Supplementary Information.

Information not provided explicitly and entirely in the manuscript is reported as Partial. This document is complementary to the manuscript to ensure all relevant information is provided.

1. Experiment overview

Item	Status	Content and location
1.1 Purpose	Reported	Develop and validate a deep-learning IFC pipeline that segments and classifies platelets, RBCs and aggregates, and apply it to four preparation methods and a pilot Long COVID cohort. Introduction, final paragraph.
1.2 Keywords	Reported	Platelets, Inflammation, Long COVID, Imaging Flow Cytometry, Deep Learning, Instance Segmentation. Abstract.
1.3 Experiment variables	Reported	Cohort: control ($n = 11$) vs Long COVID ($n = 9$). Preparation method: PRP, hematocrit, whole blood (WB) and high-yield platelet optimization (HPO). Primary endpoint: cell concentration in the HPO fraction. Methods, Demographics; Imaging Flow Cytometry.
1.4 Organization and contact	Reported	Stellenbosch University, South Africa. Corresponding author E. Pretorius, resiap@sun.ac.za. Title page.
1.5 Date	Reported	Samples collected between February and April 2024. Methods, Blood Collection Procedure.
1.6 Conclusions	Reported	Discussion, closing paragraphs. The cohort differences are exploratory and hypothesis generating.
1.7 Quality control	Reported	ASSIST calibration with calibration beads every morning before sample processing. Instrument settings kept constant during acquisition. No unstained, isotype, FMO or agonist-stimulated positive controls were included; this is not stated in the manuscript. Pipeline validated against 3000 hand-labeled images and a five-annotator panel of 50 images. Methods, Imaging Flow Cytometry; Pipeline Validation.

2. Flow sample and specimen details

Item	Status	Content and location
2.1 Sample source	Reported	Human venous blood in citrate tubes, two tubes per participant. Methods, Blood Collection Procedure.
2.2 Organism	Reported	*Homo sapiens*.
2.3 Tissue / location	Reported	Peripheral venous blood.
2.4 Age, sex, condition	Reported	Controls: 4 male, 7 female, age 37.9 ± 14.8. Long COVID: 5 male, 4 female, age 41.6 ± 14.9. Diagnosis by a medical practitioner. Comorbidities in SI Table S1. Ethics: HREC Stellenbosch University, project ID 31384; samples from the Stellenbosch University Blood Laboratory Biorepository, project ID 28804.
2.5 Sample treatment	Reported	WB: aliquoted directly. PRP: $300 \times g$, 10 min. Hematocrit: $3000 \times g$, 15 min, room temperature, plasma removed. HPO: hematocrit, complete medium (RPMI + 20% FBS) and HetaSep (STEMCELL Technologies, 07806) at 1:1:2, 140 µL incubated at 36 °C for 5 min, supernatant collected. WB and hematocrit diluted 1:1000 in PBS after staining. Methods, Blood Collection Procedure; Fluorescent Staining.

Item	Status	Content and location
2.6 Time to analysis	Reported	All laboratory methods completed on the day of collection. All samples acquired within 12 h of blood collection.
2.7 Fluorescence reagents	Reported	PAC-1, FITC, clone PAC-1, BD Biosciences 340507, RRID:AB_2230769 (activated GPIIb/IIIa). CD62P, PE, clone CLB-Thromb/6, Beckman Coulter IM1759U, RRID:AB_3755077 (P-selectin). CD235a, Brilliant Violet 421, clone HI264, BioLegend 349132 (via Biocom Africa), RRID:AB_2941527 (glycophorin A, RBC marker).
2.8 Staining volumes	Reported	PRP: 60 µL + 12 µL CD62P + 12 µL PAC-1, no CD235a. WB and hematocrit: 20 µL + 4 µL CD62P + 4 µL PAC-1 + 1 µL CD235a. HPO: 40 µL + 8 µL CD62P + 8 µL PAC-1 + 2 µL CD235a. All 30 min at room temperature, protected from light. Antibody volumes followed the manufacturers' recommendations (Methods, Fluorescent Staining). Stock concentrations: CD62P 6.25 µg/mL, PAC-1 25 µg/mL, CD235a 0.5 mg/mL. Final concentrations during staining: CD62P 0.86–0.89 µg/mL, PAC-1 3.4–3.6 µg/mL, CD235a 17 µg/mL. Antibodies were not titrated.

3. Instrument details

Item	Status	Content and location
3.1 Instrument	Reported	Amnis FlowSight imaging flow cytometer (Cytek Biosciences, Fremont, CA, USA).
3.2 Acquisition software	Reported	INSPIRE version 200.0.336.0.
3.3 Optics	Reported	$20\times$ objective; nominal pixel size 1×1 µm.
3.4 Excitation sources	Reported	405 nm laser at 80 mW; 488 nm laser at 60 mW; 785 nm side-scatter laser at 3.59 mW. No 561 nm laser. PAC-1 and CD62P excited at 488 nm, CD235a at 405 nm.
3.5 Channels	Reported	Ch01 and Ch09: brightfield. Ch02: PAC-1 FITC, 528/65 nm. Ch03: CD62P PE, 577/35 nm. Ch06: side scatter. Ch07: CD235a BV421, 457/45 nm. Methods, Imaging Flow Cytometry.
3.6 Detectors	Reported	Time delay integration (TDI) charge-coupled device cameras, 12-bit. Methods, Imaging Flow Cytometry.
3.7 Fluidics	Reported	Medium flow speed setting. Acquisition stopped after a set sample volume. HPO acquired volume 12.98–13.29 µL.
3.8 Events acquired	Reported	HPO: median 294 148 events per sample, range 194 989–453 379.

4. Data analysis details

Item	Status	Content and location
4.1 Data files	Reported	Per-object features of all 29.6 million segmented masks and the analysis code: Zenodo, 10.5281/zenodo.22895198, CC BY 4.0; code also at `https://github.com/Andreas-Wild/platelet-hyperactivation`. Segmentation model: Zenodo, restricted access, 10.5281/zenodo.22895731, PolyForm Strict 1.0.0. Raw .rif/.cif files are not deposited but are available from the corresponding author on reasonable request. Statements, Data Availability.
4.2 Compensation	Reported	Crosstalk corrected per pixel with the compensation matrix stored in each raw file, $c = S^{-1}m$. The matrix was set in INSPIRE before the study. Methods, Imaging Flow Cytometry; SI Fig. compensation matrix.
4.3 Transformation	Reported	None for analysis; median intensities in arbitrary units. Arcsinh display scale for SI image figures only.

Item	Status	Content and location
4.4 Segmentation	Reported	Cellpose3 fine-tuned on an independent IFC brightfield dataset of approximately 10 000 images (8076 training, 2016 held-out); mAP 0.665 on held-out images vs 0.143 for a Yen threshold + watershed baseline. Cellpose 3.0.9, PyTorch 2.11. Replaces IDEAS masks. Methods, Segmentation; SI.
4.5 Gating strategy	Reported	Rule-based decision tree replaces manual gates. Noise filter: brightfield SD < 8 removed. RBC-like: (major axis ≥ 7 px or equivalent diameter ≥ 8 px or CD235a median ≥ 1000) and solidity ≥ 0.88 and eccentricity ≤ 0.85. Platelet-like: small, CD235a-negative, and round or PAC-1/CD62P positive. Positivity threshold: 99th percentile of each marker among RBC-like masks per method. Touching masks (≤ 1 px apart) grouped as aggregates. Methods, Population Classification; SI Fig. decision tree.
4.6 Feature extraction	Reported	scikit-image 0.26.0 plus custom distance, connectivity and intensity features. SI feature table.
4.7 Statistics	Reported	Participant-level medians; two-sided Mann–Whitney U; BH correction; Cliff's δ. Python 3.14, SciPy 1.18.0.